REPORT

THERMOELECTRICS

Flexible thermoelectrics based on ductile semiconductors

Qingyu Yang[1,2]†, Shiqi Yang[1,2]†, Pengfei Qiu[1,3]*, Liming Peng[1,2], Tian-Ran Wei[4], Zhen Zhang[5], Xun Shi[1,2,4]*, Lidong Chen[1,2]*

Flexible thermoelectrics provide a different solution for developing portable and sustainable flexible power supplies. The discovery of silver sulfide–based ductile semiconductors has driven a shift in the potential for flexible thermoelectrics, but the lack of good p-type ductile thermoelectric materials has restricted the reality of fabricating conventional cross-plane π-shaped flexible devices. We report a series of high-performance p-type ductile thermoelectric materials based on the composition-performance phase diagram in AgCu(Se,S,Te) pseudoternary solid solutions, with high figure-of-merit values (0.45 at 300 kelvin and 0.68 at 340 kelvin) compared with other flexible thermoelectric materials. We further demonstrate thin and flexible π-shaped devices with a maximum normalized power density that reaches 30 μW cm^{-2} K^{-2}. This output is promising for the use of flexible thermoelectrics in wearable electronics.

Wearable electronics are widely used in communication, medicine, health care, and other areas, but their usage is greatly limited by the low capacity and short lifetime of power supply from chemical batteries (*1*). Therefore, portable, reliable, super-thin, and sustainable flexible power supplies are in great demand (*2*–*4*). Flexible thermoelectric (TE) generators have the advantages of small volume, no moving parts, continuously working in all weather conditions, and high reliability. They can directly convert the heat from the human body to electricity with a temperature gradient of several kelvins (or less) through the Seebeck effect, providing in principle a self-power supply solution for wearable electronics (*5*–*7*). The performance of flexible TE devices (Fig. 1A), which is usually characterized by the normalized power density ($P_{max}/A\Delta T^2$, where P_{max} is the maximum power output, A is the cross-sectional area, and ΔT is the temperature difference across the device) (*8*), is strongly dependent on the TE figure of merit (zT) of n- and p-type TE materials, as well as device integration technology. Currently, three typical approaches are used to fabricate high-performance flexible thermoelectrics. The first approach is to deposit classic brittle, inorganic, thin-film TE materials such as Bi_2Te_3–based alloys on flexible substrates or scaffolds (*9*–*11*). However, because of the difficulty in achieving dense films and/or in precisely controlling the chemical compositions, the material's zT obtained by this approach is usually low. This leads to a small normalized power density (Fig. 1B). The second approach is directly using organic TE materials to fabricate flexible devices (*12*). Unfortunately, because of their poor electrical transport, the zTs of organic TE materials (Fig. 1C), particularly for n-type materials (*13*, *14*), are much lower than those for state-of-the-art inorganic TE materials. This also leads to very low normalized power density, on the order of 10^{-3} to 10^{-5} μW cm^{-2} K^{-2} (Fig. 1B) (*15*, *16*).

Recently discovered ductile TE semiconductors provide a third avenue for high-performance flexible thermoelectrics because of their excellent metal-like machinability. Inorganic Ag_2S–based materials and InSe single crystals with good ductility and tunable electrical properties have been reported (*17*, *18*). After this development, $Ag_2(Se,Te,S)$–based materials with both high zT and inherent ductility were developed, pushing the zT value of n-type ductile TE materials to 0.44 at room temperature, which is among the highest values in flexible TE materials (Fig. 1C). However, the current zT value of p-type ductile TE materials

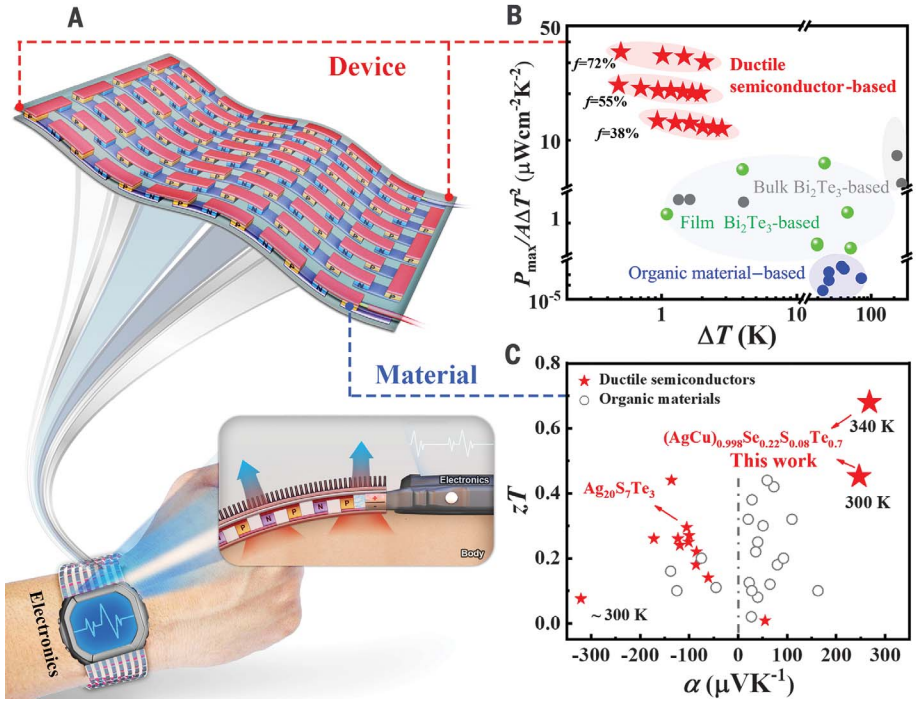

Fig. 1. Flexible TE materials and devices. (**A**) Schematics of flexible thermoelectrics that could be used in wearable electronics with a cross-plane π-shaped structure. (**B**) Normalized power density ($P_{max}/A\Delta T^2$) of flexible TE devices achieved by using ductile materials with different filling factors (*f*). Data for Bi_2Te_3 film–based devices, organic material–based devices, and traditional Bi_2Te_3–based bulk devices are included for comparison. (**C**) Room-temperature thermoelectric figure of merit (zT) and Seebeck coefficient (α) for ductile inorganic materials and organic-based materials. The detailed data in (B) and (C) and the related references are listed in tables S1 and S2.

[1]State Key Laboratory of High Performance Ceramics and Superfine Microstructure, Shanghai Institute of Ceramics, Chinese Academy of Sciences, Shanghai 200050, China. [2]Center of Materials Science and Optoelectronics Engineering, University of Chinese Academy of Sciences, Beijing 100049, China. [3]School of Chemistry and Materials Science, Hangzhou Institute for Advanced Study, University of Chinese Academy of Sciences, Hangzhou 310024, China. [4]State Key Laboratory of Metal Matrix Composites, School of Materials Science and Engineering, Shanghai Jiao Tong University, Shanghai 200240, China. [5]Division of Solid-State Electronics, Department of Electrical Engineering, Uppsala University, 75103 Uppsala, Sweden.
***Corresponding author. Email: qiupf@mail.sic.ac.cn (P.Q.); xshi@mail.sic.ac.cn (X.S.); cld@mail.sic.ac.cn (L.C.)**
†These authors contributed equally to this work.

at room temperature is still very poor (0.01 at 300 K) (*19*). Thus, the fabrication of flexible TE devices based on ductile TE semiconductors with the conventional, and often most practical, cross-plane π-shaped structure (Fig. 1A) are quite challenging because of the lack of good p-type ductile TE materials. We report a series of high-performance p-type ductile TE materials, AgCu(Se,S,Te) pseudoternary solid solutions, with a zT of 0.45 at 300 K and 0.68 at 340 K, attractive values for flexible TE materials (Fig. 1C). We successfully developed the flexible π-shaped TE devices (0.3 mm thick) based on inorganic materials, with a maximum normalized power density up to 30 μW cm^{-2} K^{-2}. This value is about four times that of the Bi_2Te_3–based TE devices (*20*–*22*), at least four orders of magnitude higher than that of organic-based flexible TE devices (Fig. 1B) (*13*–*15*), and one order of magnitude higher than that of other low-grade heat-to-electricity conversion technologies (*8*, *23*, *24*).

The phase diagram and chemical defects are quite complicated in the (Ag, Cu)-X (X = S, Se, Te) family, which includes Ag_2X, AgCuX, and their derivatives, and also provides an opportunity for tuning their transport and mechanical properties through composition and structure modulation. Generally, Ag-contained compounds are n-type, whereas Cu-contained ones are p-type; a high S content or a high Ag content tends to result in ductile materials, whereas high Se and Te contents or high Cu content are prone to be brittle materials (*19*). We focused on AgCu(Se,S,Te) pseudoternary solid solutions in an attempt to find high-performance p-type ductile TE materials. We use a composition-performance phase diagram to show the relationship that we obtained experimentally (Fig. 2). Additional details on the crystal structures and phase compositions of AgCu(Se,S,Te) pseudoternary solid solutions can be found in the supplementary materials and in figs. S1 to S3. AgCuSe is brittle and shows n-type conduction, with a maximum bending deformation of ~3% in the three-point bending test (fig. S4A). Alloying Te in AgCuSe does not change the brittle feature (fig. S4A) but does convert the electrical conduction to p-type. The boundary of p/n conductions in AgCu($Se_{1-y}Te_y$) is ~y = 0.5 (fig. S5). Upon further alloying a tiny amount of S in AgCu($Se_{1-y}Te_y$) (0.7 ≥ y ≥ 0.5), a "brittle-ductile" transition occurred, and we obtained ductile p-type materials in AgCu($Se_{1-y-x}S_xTe_y$) with x between 0.05 and 0.08 and y between 0.5 and 0.7 (Fig. 2).

$AgCuSe_{0.3-x}S_xTe_{0.7}$ (x = 0.06 and 0.08) are ductile and plastic materials, as determined with mechanical tests (Fig. 3, A and B). Room temperature compression and three-point bending tests showed strain values of >30% and 10%, respectively, which are comparable to ductile Ag_2S and its derivates (*17*, *25*, *26*). We also observed a similar metal-like ductility in other AgCu($Se_{1-y-x}S_xTe_y$) pseudoternary solid solutions over a broad composition range, such as $AgCuSe_{0.5-x}S_xTe_{0.5}$ (x = 0.05 and 0.07), $AgCuSe_{0.35}S_{0.05}Te_{0.6}$ (fig. S4B), and cation-deficient $(AgCu)_{1-\delta}Se_{0.22}S_{0.08}Te_{0.7}$ (δ = 0.002) (Fig. 3, A and B).

We used $AgCuSe_{0.22}S_{0.08}Te_{0.7}$, which has the highest zT among all of the fabricated p-type materials tested (Fig. 2), as the typical example to perform the detailed microstructure characterization. After compression tests, we observed obvious slip bands along different directions on the material's surface, indicating the existence of multiple slip bands (Fig. 3C). Inside each slip band, we observed numerous finer slip lines (fig. S6A). The space between the nearby parallel slip lines was dozens of nanometers. In addition, numerous dimples with sizes ranging from several hundred nanometers to several micrometers appeared on the fracture surface of $AgCuSe_{0.22}S_{0.08}Te_{0.7}$ (Fig. 3D), which was different from the river-like patterns on the fracture surface of brittle $AgCuSe_{0.3}Te_{0.7}$ (fig. S6B). Similar to many metals, these dimples are considered to be produced by the nucleation, growth, and aggregation of the microscopic cavity during plastic deformation (*27*, *28*). Because of their good ductility, the AgCu(Se,S,Te) materials can be easily machined to flexible films with a thickness down to 100 μm (Fig. 3E).

The good ductility of $AgCuSe_{0.3-x}S_xTe_{0.7}$ (x = 0.06 and 0.08) comes from the alloyed S, even though the content is very low. The engineering strain was just 3% for S-free $AgCuSe_{0.3}Te_{0.7}$ in the three-point bending test, but was substantially enhanced to ~13 and 18% by alloying S contents of 0.06 and 0.08, respectively (Fig. 3F). We observed a similar phenomenon in S-alloyed $AgCuSe_{0.5}Te_{0.5}$ (fig. S4, A and B). To understand the underlying reason for this sort of brittle-ductile transition, we calculated the slipping energy barrier (E_b) and cleavage energy (E_c) of S/Te–alloyed AgCuSe. The E_b along the (010)[100] slip system was almost unchanged upon alloying either S or Te; however, the E_c was obviously increased upon alloying S but decreased upon alloying Te (fig. S7). The enhanced ratio of E_c/E_b caused by the increased amount of multicentered and diffused Ag–S bonds (*17*) is beneficial for the material's slip before fracture.

Beyond the attractive ductility, $AgCuSe_{0.3-x}S_xTe_{0.7}$ (x = 0.06 and 0.08) showed p-type conduction with relatively good TE properties. We measured a positive Seebeck coefficient α (fig. S8A) and Hall coefficients R_H (fig. S8B), indicating the p-type conduction behavior. Upon alloying S, the α was enhanced but the electrical conductivity σ was lowered (fig. S8, A and C) because of the lowered hole concentration p_H (fig. S8D). Because the Ag–S bond is more ionic than Ag–Se and Ag–Te bonds, the Cu-deficiency defects were greatly suppressed when alloying S, leading to the decreased reduced Fermi energy (fig. S8E) and hole concentrations. Likewise, both carrier thermal conductivity (κ_C) and lattice thermal conductivity (κ_L) were also reduced upon alloying S (fig. S8F), yielding the lowered thermal conductivity κ (fig. S8G). The power factors (PF = $\alpha^2\sigma$) of $AgCuSe_{0.3-x}S_xTe_{0.7}$ (x = 0.06 and 0.08) were ~3 μW cm^{-1} K^{-2} (fig. S8H), whereas the thermal conductivities κ (fig. S8G) were only ~0.3 to 0.4 W m^{-1} K^{-1}, leading to a zT of up to

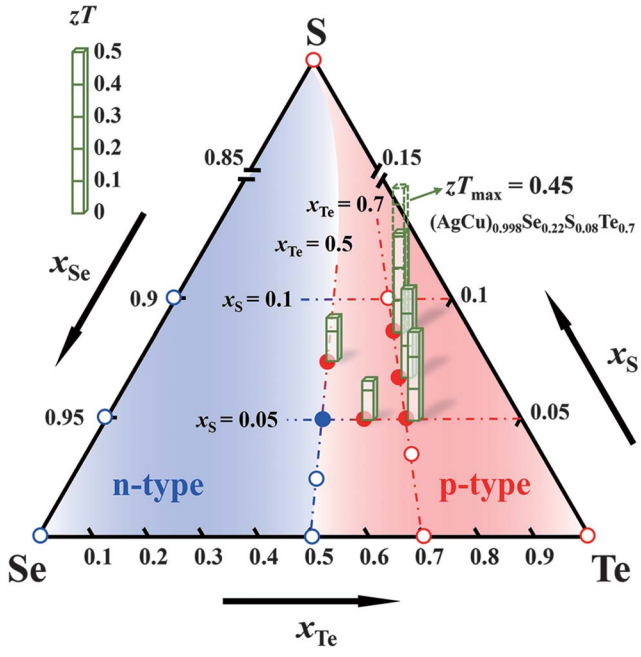

Fig. 2. Composition-performance phase diagram of AgCuSe-AgCuS-AgCuTe pseudoternary solid solutions. Columns represent zT at room temperature. Blue and red symbols represent n- and p-type conduction, respectively. Filled circles represent ductile compositions and hollow circles brittle compositions.

0.31 at 300 K (Fig. 3G). Upon further introducing a tiny amount of cation deficiency, we were able to enhance the *PF* to 5.1 μW cm^{-1} K^{-2} at 300 K (fig. S8H). Although the κ of cation deficient material was slightly enhanced because of the increased κ_C (fig. S8, F and G), the *zT* was still improved to 0.45 at 300 K and 0.68 at 340 K (Fig. 3G) for $(AgCu)_{0.998}Se_{0.22}S_{0.08}Te_{0.7}$, respectively. Likewise, good reproducibility of TE properties was observed in our ductile TE materials (fig. S9).

The *zT* values of our ductile semiconductors were much higher than those of organic materials (Fig. 1C), even close to the commercial zone-melted Bi_2Te_3–based alloys. These high *zT* values can be mainly attributed to their ultralow κ_L originating from the severe atomic-lattice disorders caused by the complex chemical compositions (*29*). The κ of ductile $AgCuSe_{0.3-x}S_xTe_{0.7}$ (x = 0.06 and 0.08) was much lower than that of the classic Bi_2Te_3–based materials (1.0 to 1.8 Wm^{-1} K^{-1} at 300 K) (*21*), and was even comparable to that of wood (0.1 to 0.3 W m^{-1} K^{-1}) (*30*). Such an ultralow κ is helpful for realizing a large temperature gradient across a TE device. In addition, ductile TE materials have larger α and *PF* than the organic TE materials (Fig. 3H), which is beneficial for achieving high onset voltage with fewer p/n couples in TE devices.

The discovery of high-performance n- and p-type ductile TE materials offers the opportunity to fabricate flexible cross-plane π-shaped TE devices (Fig. 4A). We selected p-type $(AgCu)_{0.998}Se_{0.22}S_{0.08}Te_{0.7}$ and n-type $Ag_{20}S_7Te_3$ (Fig. 1C) to connect electrically in series and thermally in parallel between two polyimide (PI)–based flexible circuit boards. Taking advantage of the materials' ductility, we cut n- and p-type ultra-thin plates with a thickness of 0.1 mm directly from bulk ingots. The intrinsic brittleness of traditional thermoelectric alloys such as the Bi_2Te_3–based ones prevents fabricating a similar thickness in these materials. We metallized the thin plates by magnetron sputtering using tungsten (W) and tin (Sn) as contact layers with an electrical contact resistivity (ρ_c) of 19 and 2 μΩ cm^2 for Sn/W/$(AgCu)_{0.998}Se_{0.22}S_{0.08}Te_{0.7}$ and Sn/W/$Ag_{20}S_7Te_3$ interfaces (Fig. 4B), respectively. These small ρ_c values, as well as the large thermal conductivities of W and Sn, suggest that the additional thermal resistance introduced by the contact layer was very low. The metalized thin films were cut into the assigned shapes and then soldered onto the Cu/Au electrodes in PI-based flexible circuit boards using a low-temperature solder paste (fig. S10A).

We successfully fabricated a few flexible cross-plane π-shaped TE devices with six-couple $(AgCu)_{0.998}Se_{0.22}S_{0.08}Te_{0.7}$/$Ag_{20}S_7Te_3$ legs (Fig. 4C). We designed the same dimensions of TE legs but different filling factors (*f*) with the values of 38, 55, and 72%. The total thickness

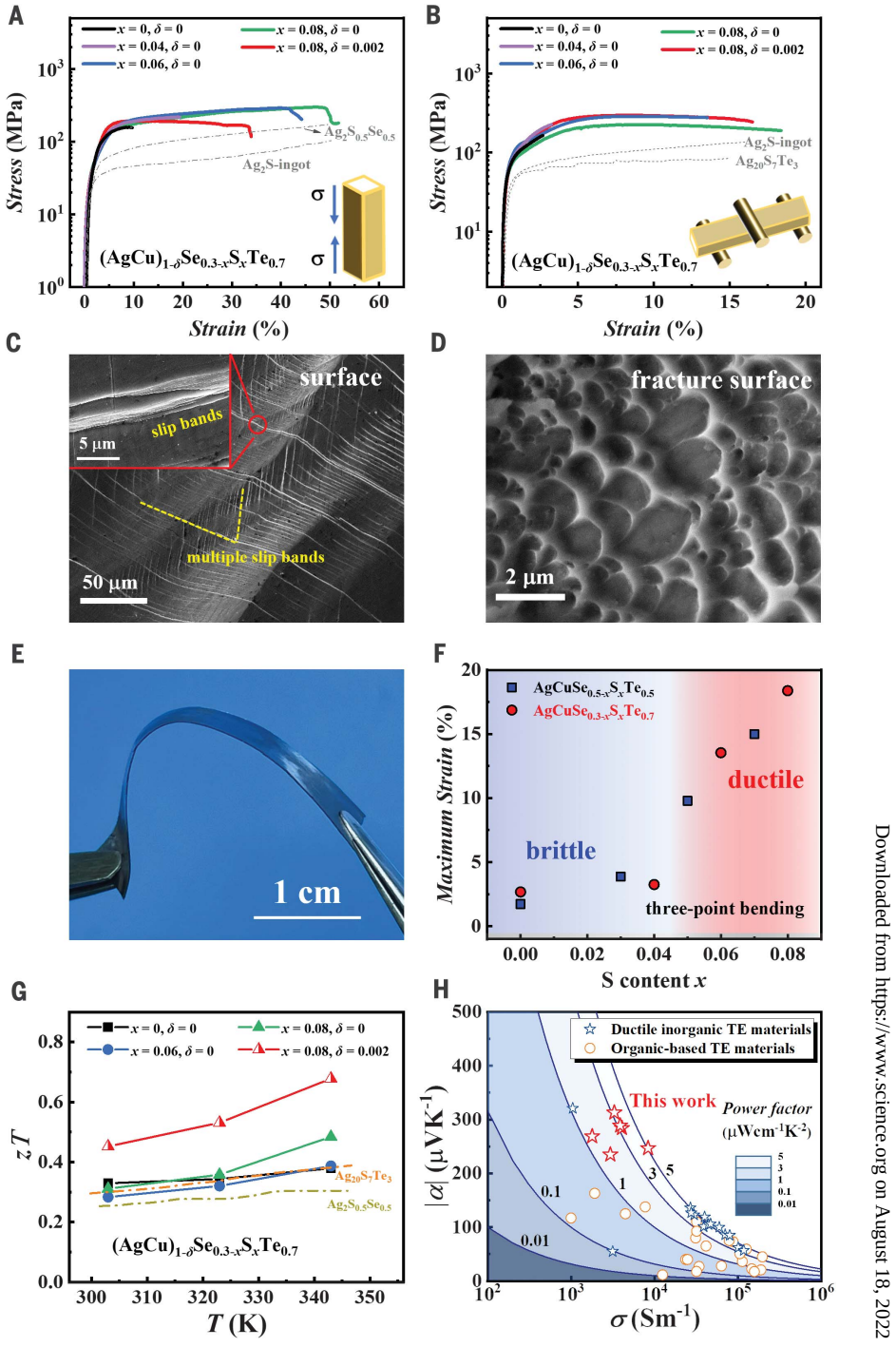

Fig. 3. Mechanical and thermoelectric properties of $(AgCu)_{1-\delta}Se_{0.3-x}S_xTe_{0.7}$. (**A** and **B**) Engineering stress-strain curves for compression (A) and bending (B) tests for $(AgCu)_{1-\delta}Se_{0.3-x}S_xTe_{0.7}$ (x = 0, 0.04, 0.06, and 0.08; δ = 0 and 0.002) at room temperature. Data for Ag_2S and its n-type derivates are included for comparison (*17*, *25*, *26*). (**C** and **D**) SEM images of the surface (C) and fracture surface (D) of $AgCuSe_{0.22}S_{0.08}Te_{0.7}$ after the compression test. (**E**) Optical image of the $AgCuSe_{0.22}S_{0.08}Te_{0.7}$ thin film showing good flexibility. (**F**) Maximum engineering strains of bending test as a function of S content for $AgCuSe_{0.5-x}S_xTe_{0.5}$ and $AgCuSe_{0.3-x}S_xTe_{0.7}$. (**G**) Temperature dependence of TE *zT* for $(AgCu)_{1-\delta}Se_{0.3-x}S_xTe_{0.7}$ (x = 0, 0.06, and 0.08; δ = 0 and 0.002). (**H**) Absolute value of Seebeck coefficient (α) as a function of electrical conductivity (σ) for p-type AgCu(Se,S,Te) ductile TE materials. Data for n-type Ag_2S-based ductile materials and typical organic-based TE materials are included for comparison. The detailed data in (H) and the related references are listed in table S1.

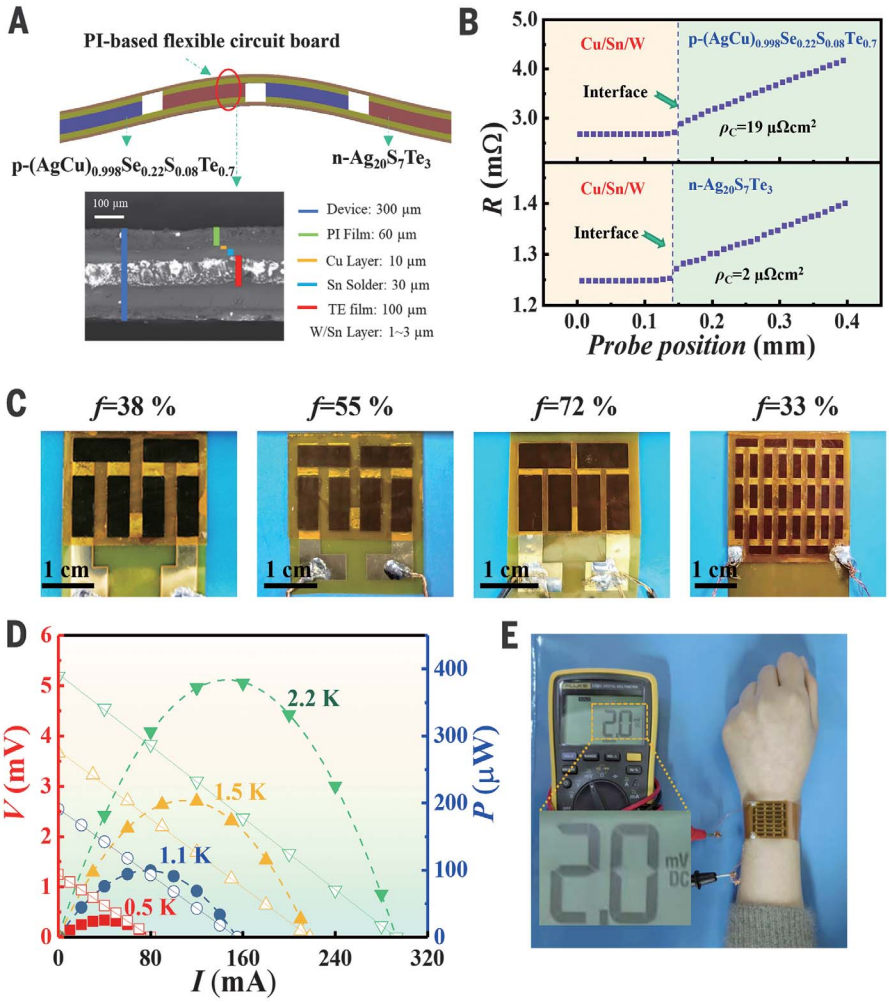

Fig. 4. Super-thin flexible TE devices based on ductile semiconductors. (**A**) Structure of the π-shaped flexible $(AgCu)_{0.998}Se_{0.22}S_{0.08}Te_{0.7}/Ag_{20}S_7Te_3$ TE device. The bottom panel is the SEM image for the overall cross-section of the flexible device with the thicknesses of each layer labeled. (**B**) Resistance (*R*) line scanning across the interface for the p- and n-type TE elements. (**C**) Optical images of the as-prepared six-couple flexible TE devices with different filling factors (*f* = 38, 55, and 72%) and 31-couple flexible TE devices (*f* = 33%). (**D**) Measured output voltage (*V*) and output power (*P*) as a function of current (*I*) under different temperature differences for the six-couple $(AgCu)_{0.998}Se_{0.22}S_{0.08}Te_{0.7}/Ag_{20}S_7Te_3$ flexible TE device with *f* = 72%. (**E**) Optical image of the 31-couple flexible TE device adhered on a human's wrist.

of our flexible TE was only 0.3 mm with an upper limit of several millimeters, like a normal rigid device. Therefore, the thickness of our flexible device can be freely tuned from 0.3 mm to a few millimeters. We characterized the performance of these devices using a home-made test platform (fig. S10B). We show the output voltage (*V*) and output power (*P*) as a function of current (*I*) under different ΔT for the device with *f* = 72% in Fig. 4D. The device internal resistance (R_{in}) was ~18 mΩ, which is comparable to the theoretical value (19 mΩ) calculated on the basis of the material's electrical resistance. This R_{in} was at least three orders of magnitude lower than that of flexible organic material-based TE devices (*14*, *15*) and two orders of magnitude lower than that of classic bulk Bi_2Te_3–based TE devices (fig. S11). Such low R_{in}, caused by the super-thin TE legs, is beneficial for achieving super-high output power *P*. The open circuit voltage (V_{OC}) and maximum output power ($P_{max} = V_{OC}^2/4R_{in}$) increased with increasing ΔT, reaching 3.7 mV and 203 μW at ΔT =1.5 K (Fig. 4D), respectively. The maximum normalized power density $P_{max}/A\Delta T^2$ was ~30 μW cm^{-2} K^{-2}, a high value compared with other reported flexible TE devices and even bulk TE devices (Fig. 1B) (*14*–*16*, *20*–*22*).

We also tested the performance of the devices with *f* = 38% and *f* = 55% (fig. S12, A and B). Under similar ΔT, the device with higher *f* had higher V_{OC}/A and $P_{max}/A\Delta T^2$ (fig. S12, C and D). The $P_{max}/A\Delta T^2$ values were ~13 and 20 μW cm^{-2} K^{-2} when *f* = 38 and 55%, respectively, still much higher than that of current TE devices (Fig. 1B) (*14*–*16*, *20*–*22*). Such ultrahigh performances are mainly caused by the material's high TE figure of merit, short length of TE legs, and low energy loss at the material/electrode interfaces.

The super-thin and highly efficient flexible TE devices developed in this study can be implemented into the Internet of Things, quartz watches, or motion detectors, acting as a charge-free battery to monitor human health or the environment. Toward these potential applications, we fabricated a cross-plane π-shaped TE device including 31-couple $(AgCu)_{0.998}Se_{0.22}S_{0.08}Te_{0.7}/Ag_{20}S_7Te_3$ with *f* = 33% (Fig. 4C, right). This device can easily and effectively adhere to the curved surface of human skin using adhesive tape (Fig. 4E). Under an ambient temperature of 298 K and humidity of 42%, directly adhering the device on a human's wrist gave a V_{OC} and P_{max} of 0.2 mV and 70 nW, respectively (fig. S13A). The $P_{max}/A\Delta T^2$ of this device was ~11 μW cm^{-2} K^{-2}, the same as for the six-couple device with a similar filling factor. By shaking the arms to strengthen the convective heat transfer, the ΔT across the TE device could be enhanced to 0.1 K to yield a V_{OC} and P_{max} of 0.76 mV and 1 μW, respectively (fig. S13B). Spraying alcohol on the device's upper surface could cause a large ΔT (0.35 K), yielding a high V_{OC} and P_{max} of 2.5 mV and 13 μW, respectively (fig. S13C). In real applications, various heat-dissipation approaches (e.g., copper pipes and graphite sheets) will be applied to further enhance ΔT to 1 to 2 K to reach the threshold of 100 μW, which is strong enough to power many microelectronics such as quartz watches and wireless sensor nodes. Furthermore, the total thickness of our flexible device can be freely tuned for various working conditions with different temperature gradients and working spaces.

We also tested the service stability of our flexible TE device by cyclically bending the 31-couple device with a filling factor of 33% under a bending radius of 15 mm. After bending 500 times, the relative inner resistance ($R_{in}/R_{in,0}$) was scarcely changed (fig. S13D). A service stability test was also performed in two long-strip-shaped devices with high filling factors of 55 and 71%. The maximum increment of $R_{in}/R_{in,0}$ was <5% after bending 500 times (fig. S13, E to G). These tests indicate that the service stability of our device is acceptable. Furthermore, we found that humidity had little influence on the V_{OC} and P_{max} of the device (fig. S13H).

In summary, we have discovered p-type ductile TE materials with a relatively high TE figure of merit compared with other flexible materials. Coupled with high-performance

n-type ductile materials, we successfully developed super-thin flexible TE devices with a conventional π-shape, ultra-high normalized power density, and reasonable service stability. Ductile semiconductors thus provide a different strategy for high-performance flexible thermoelectrics, which can directly and efficiently convert low-grade heat energy such as the heat from human body into useful and sustainable electricity. Our study offers a promising example of applying a self-powered supply technology to wearable electronics.

REFERENCES AND NOTES

1. J. M. Tarascon, M. Armand, *Nature* **414**, 359–367 (2001).
2. S. Park *et al*., *Nature* **561**, 516–521 (2018).
3. D. P. Dubal, N. R. Chodankar, D. H. Kim, P. Gomez-Romero, *Chem. Soc. Rev.* **47**, 2065–2129 (2018).
4. W. Gao *et al*., *Nature* **529**, 509–514 (2016).
5. K. Nan *et al*., *Sci. Adv.* **4**, eaau5849 (2018).
6. C. Wan *et al*., *Nat. Mater.* **14**, 622–627 (2015).
7. Y. Wang *et al*., *Adv. Mater.* **31**, e1807916 (2019).
8. X. Shi, J. He, *Science* **371**, 343–344 (2021).
9. Q. Jin *et al*., *Nat. Mater.* **18**, 62–68 (2019).
10. S. J. Kim *et al*., *ACS Nano* **10**, 10851–10857 (2016).
11. S. J. Kim, J. H. We, B. J. Cho, *Energy Environ. Sci.* **7**, 1959–1965 (2014).
12. G. H. Kim, L. Shao, K. Zhang, K. P. Pipe, *Nat. Mater.* **12**, 719–723 (2013).
13. C. Y. Yang *et al*., *Nat. Commun.* **11**, 3292 (2020).
14. Y. Sun *et al*., *Adv. Mater.* **24**, 932–937 (2012).
15. T. Sun *et al*., *Nat. Commun.* **11**, 572 (2020).
16. O. Bubnova *et al*., *Nat. Mater.* **10**, 429–433 (2011).
17. X. Shi *et al*., *Nat. Mater.* **17**, 421–426 (2018).
18. T. R. Wei *et al*., *Science* **369**, 542–545 (2020).
19. Z. Gao *et al*., *Adv. Energy Mater.* **11**, 2100883 (2021).
20. C. S. Kim *et al*., *ACS Energy Lett.* **3**, 501–507 (2018).
21. R. Deng *et al*., *Energy Environ. Sci.* **11**, 1520–1535 (2018).
22. F. Suarez *et al*., *Appl. Energy* **202**, 736–745 (2017).
23. C. G. Han *et al*., *Science* **368**, 1091–1098 (2020).
24. B. Yu *et al*., *Science* **370**, 342–346 (2020).
25. J. Liang *et al*., *Energy Environ. Sci.* **12**, 2983–2990 (2019).
26. S. Yang *et al*., *Adv. Mater.* **33**, 2007681 (2021).
27. J. P. Bandstra, D. A. Koss, A. Geltmacher, P. Matic, R. K. Everett, *Mater. Sci. Eng. A* **366**, 269–281 (2004).
28. S. He *et al*., *Sci. Adv.* **6**, eaaz8423 (2020).
29. H. Liu *et al*., *Nat. Mater.* **11**, 422–425 (2012).
30. B. M. Suleiman, J. Larfeldt, B. Leckner, M. Gustavsson, *Wood Sci. Technol.* **33**, 465–473 (1999).

ACKNOWLEDGMENTS

We thank Z. Zhou for help with crystal structure analysis. **Funding:** This work was supported by the National Natural Science Foundation of China (grants 91963208, 52122213, and 51625205), the Shanghai Government (grants 20JC1415100 and JCYJ-SHFY-2022-002), and the CAS-DOE Program of the Chinese Academy of Sciences (grant 121631KYSB20180060). Z.Z. is supported by the Swedish Research Council (grant VR 2018-06030). **Author contributions:** Q.Y. prepared the samples and measured the thermoelectric and mechanical properties. S.Y. and L.P. fabricated the devices and measured the output performance. Q.Y., S.Y., L.P., and T.W. collected the data and interpreted the results under the guidance of P.Q., X.S., and L.C.. Q.Y., S.Y., P.Q., Z.Z., X.S., and L.C. wrote the paper. All authors discussed the results and provided helpful suggestions. **Competing interests:** The authors declare no competing interests. **Data and materials availability:** All data are available in the manuscript or the supplementary materials.

SUPPLEMENTARY MATERIALS

science.org/doi/10.1126/science.abq0682
Materials and Methods
Supplementary Text
Figs. S1 to S13
Tables S1 to S4
References (*31*–*64*)

Submitted 15 March 2022; accepted 28 June 2022
10.1126/science.abq0682

Flexible thermoelectrics based on ductile semiconductors

Qingyu YangShiqi YangPengfei QiuLiming PengTian-Ran WeiZhen ZhangXun ShiLidong Chen

Science, 377 (6608), • DOI: 10.1126/science.abq0682

A flexible power source

Thermoelectric materials can harvest heat and turn it into power. Heat sources potentially include the heat generated by humans through wearable devices and might enable self-powering systems, but the lack of ductility for most thermoelectrics poses a major problem. Yang *et al*. found a thermoelectric silver/copper–based semiconductor that also is ductile (see the Perspective by Hou and Zhu). This material allows for a thin, flexible device capable of producing power, even when adhered to a wrist. —BG